



Evaluation of WRF land surface schemes in land-atmosphere exchange simulations over grassland in Southeast Tibet

Shupo Ma^a, Libo Zhou^{a,b,*}, Fei Li^a, Jinhuan Zhu^a

^a Department of Lower Atmosphere Observation Research (LAOR), Institute of Atmospheric Physics, Chinese Academy of Sciences, Beijing 100029, China

^b State Key Laboratory of Atmospheric Boundary Layer Physics and Atmospheric Chemistry (LAPC), Institute of Atmospheric Physics, Chinese Academy of Sciences, Beijing 100029, China

ARTICLE INFO

Keywords:

The Tibetan Plateau
The Weather Research and Forecasting (WRF) model
Land surface schemes (LSSs)
The South Asian summer monsoon (SASM)
Land-atmosphere exchange processes

ABSTRACT

Land surface schemes (LSSs) evaluation is essentially important for land-atmosphere energy exchange simulation over the Tibetan Plateau (TP), especially over the Southeast Tibet, where the atmospheric systems of the TP and South Asia interact most. In May 20–July 9, 2013, an observation was conducted over the grassland in the Southeast Tibet, with radiation, sensible, latent and ground heat fluxes measured. Based on the observation data, all seven WRF (the Weather Research and Forecasting Model) coupled LSSs (SLAB, Noah, RUC, Noah-MP, CLM, PX, SSIb) were assessed. All the LSSs can successfully reproduce the diurnal variation of land-atmosphere heat transfer but with amplitude differences from observations. The LSSs also reproduced the variations of land-atmosphere exchange processes under different synoptic situations, especially at the South Asian summer monsoon (SASM) south and north phases. However, large magnitude differences exist within the LSSs simulations in comparison with the observations, which complicated our scheme evaluations and optimal LSSs selections for the Southeast Tibet. Further quantitative studies revealed that the WRF-Noah scheme performed the best among all seven LSSs in retrieving the land-atmosphere heat transfer, partly due to its most successful surface temperature simulation. Our results suggest that the WRF-Noah scheme should be applied for future land-atmosphere exchange simulations over the Southeast Tibet.

1. Introduction

The Tibetan Plateau (TP) is the highest plateau in the world with an average altitude of over 4000 m. Strong solar radiation on elevated surfaces can drive distinct land-atmosphere exchange processes over the plateau, which then strongly affect the weather, climate, and environment in the Northern Hemisphere (Ye and Gao, 1979; Tao et al., 1999; Wu et al., 2007, 2017; Zhou et al., 2011, 2012, 2015). Ye and Gao (1979), Wu and Zhang (1998), and Wu et al. (2012) revealed a strong land-atmosphere heat exchange over the TP during the spring-summer season, which is dominated by the sensible heat transfer. Tao et al. (1999), Duan and Wu (2008), and Zhou et al. (2015) further showed the important role of latent heat transfer in the land-atmosphere heat exchange during the wet season. Zou (1996), Zou and Gao (1997) and Zhou et al. (2013) found that the strong plateau heat transfers could result in an ozone low over the TP. Thus, investigating these land-atmosphere heating processes is a key focus for TP research.

The Weather Research and Forecasting (WRF) Model is a state-of-

the-art regional modeling system (Skamarock et al., 2008) and is widely used in the mesoscale and regional scale atmospheric research. Many studies use the WRF model to investigate the land-air exchange processes in different regions with different land surface schemes (LSSs) (Hong et al., 2009; Miao et al., 2009; Jin et al., 2010; Porter et al., 2012; Lin and Cheng, 2016; Yang et al., 2017). These studies indicate that the performance of WRF LSSs varies with regions. However, due to the lack of observation data, only a few studies focused on the performances of WRF LSSs over the TP. Maussion et al. (2011) simulated the precipitation over TP using the WRF-Noah scheme. Gao et al. (2017) showed that the WRF Noah-MP scheme seemed to perform better than the WRF Noah scheme over the TP for near-surface energy fluxes and air temperature. They also emphasized that the selection of LSMs was crucially important for dynamical downscaling modeling over the TP. Xu et al. (2019) assessed the eight WRF boundary layer schemes with Noah LSS in the Central TP, and reported that different boundary layer schemes showed different performances for different observation sites and meteorological parameters. Given the large discrepancy of WRF

* Corresponding author at: Department of Lower Atmosphere Observation Research (LAOR), Institute of Atmospheric Physics, Chinese Academy of Sciences, Beijing 100029, China.

E-mail addresses: mashupo@mail.iap.ac.cn (S. Ma), zhoulibo@mail.iap.ac.cn (L. Zhou), lfei@mail.iap.ac.cn (F. Li), zhujinhuan@mail.iap.ac.cn (J. Zhu).

<https://doi.org/10.1016/j.atmosres.2019.104739>

Received 7 May 2019; Received in revised form 27 October 2019; Accepted 27 October 2019

Available online 01 November 2019

0169-8095/ © 2019 Elsevier B.V. All rights reserved.

LSSs over different TP regions, the schemes should be evaluated before their applications to the land-atmosphere exchange processes simulations over a specific TP region.

The Southeast Tibet is a key region where the plateau and South Asian atmosphere interacts most. Studies showed that the local heat transfer, as well as the radiation conditions, over the Southeast Tibet, were strongly affected by the South Asian summer monsoon (SASM) (Zou et al., 2009, 2012; Zhou et al., 2012, 2015). Evaluations of the different WRF LSSs over the Southeast Tibet are thus essential not only for better understanding the land-atmosphere exchange processes over the plateau region but also the interaction between the plateau's atmosphere and South Asian climate systems. During May–July 2013, an observation was conducted in the Southeast Tibet, with the land-atmosphere heat fluxes measured, which provided an opportunity to assess the different LSSs and optimal selection of best scheme suitable for land-atmosphere exchange processes simulation in Southeast Tibet. This work may also provide information to model developers and users for the improvement and application of the WRF over the TP region. The paper is organized as follows: the model, LSSs and observational data are described in Section 2, the performances of different LSSs and their evaluations are presented in Section 3, discussions and conclusions are given in Sections 4 and 5, respectively.

2. Methods and data

2.1. Model descriptions and experiments setting

The WRF (ARW) version 3.6.1 was used in this study, which was developed by various research institutes and universities including the National Center for Atmospheric Research (NCAR), the National Center for Environmental Prediction (NCEP), the Forecast Systems Laboratory (FSL), the Air Force Weather Agency (AFWA), etc. The WRF is the next-generation mesoscale numerical weather prediction system and serves a wide range of meteorological applications from small to large scales (Skamarock et al., 2008).

To evaluate the performances of WRF LSSs in simulating the land-atmosphere interaction in Southeast Tibet, we conducted seven experiments with the SLAB (5-layer thermal diffusion; Dudhia, 1996), Noah (Chen and Dudhia, 2001), RUC (Benjamin et al., 2004), Noah-MP (Niu et al., 2011), CLM (Lawrence et al., 2011), PX (Pleim and Xiu, 1995; Xiu and Pleim, 2001) and SSiB (Xue et al., 1991) LSSs. Except the differences among LSSs, all experimental runs used the same physical parameterizations as briefly summarized in Table 1.

Three model domains with two-way nesting were used, with horizontal grid spacings of 15, 3, and 1 km (Fig. 1) and grid numbers of 83 × 83, 91 × 91, 94 × 94, respectively. All domains had 45 vertical levels from surface to 50 hPa. The first model level is approximately 38 m above the ground for the observation site, with 12 levels below 2000 m above ground level. To keep the model steady and efficient, we used the adaptive timestep for the simulations. For the outer domain, the timestep varied between 30 s and 105 s, and for the most inner domain, the timestep varied between 1 s and 4 s. All runs used the U.S. Geological Survey (USGS) 24-category vegetation dataset, except for the run with the SSiB scheme, which used the “SSiB_5m land use

Table 1
Physical parameterization schemes used in this study.

Physics option	Parameterization scheme
Cumulus parameterization	Kain-Fritsch (Kain, 2004) for the outer domain
Microphysics	New Thompson scheme (Thompson et al., 2008)
Long- and short-wave radiation	RRTMG (Iacono et al., 2008)
Surface drag	UW (Mass and Owens, 2011)
Boundary layer	YSU (Hong et al., 2006)
Surface layer	Revised MO scheme (Jiménez et al., 2012)

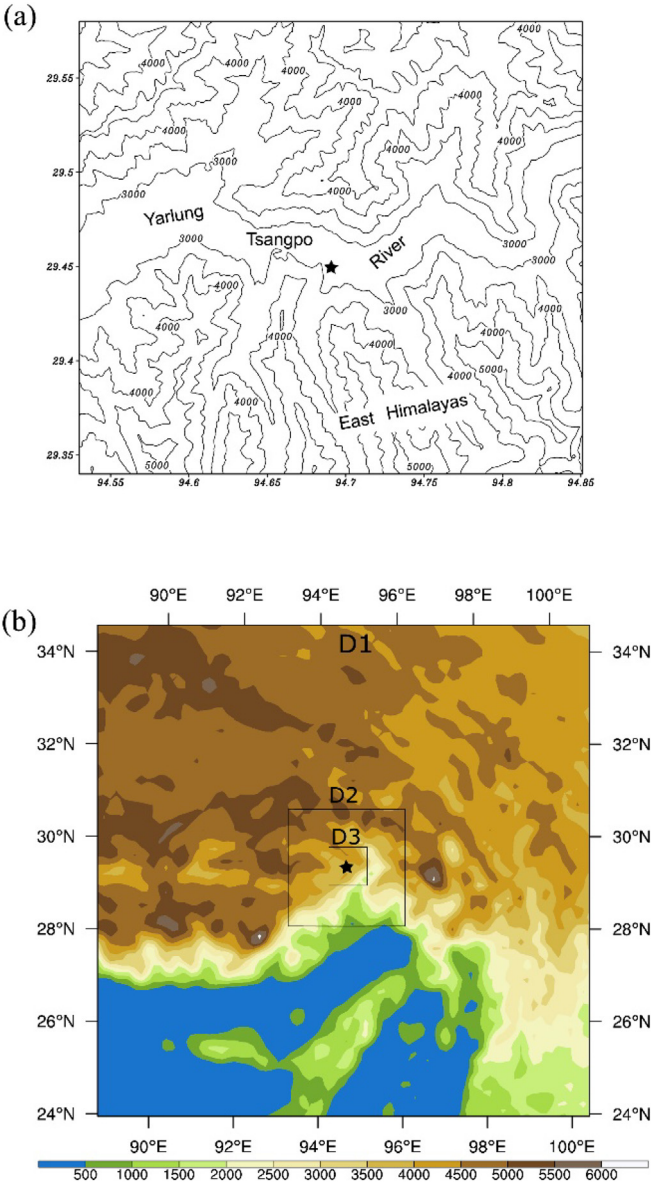


Fig. 1. Topography of the observation sites (a), and the model domains (b).

dataset”. The NCEP Climate Forecast System Version 2 (CFSv2) 6-h Product (Saha et al., 2011) with a horizontal resolution of 0.5° × 0.5° was used for initial and boundary conditions. We found the soil moisture of the CFSv2 data was much larger than the observations. Previous studies suggested that the Global Land Data Assimilation System (GLDAS; Rodell et al., 2004) is suitable for studying the soil moisture conditions in the Tibetan Plateau (e.g., Chen et al., 2013; Liu et al., 2015). In this study, the GLDAS version 2 data produced by the Noah model, with a spatial resolution of 0.25° × 0.25°, and temporal resolution of 6-hourly was used.

Three statistical quantities were calculated to evaluate the models' performances: mean bias (MB), root-mean-square error (RMSE), and correlation coefficient (COR). They are defined as follows:

$$MB = \frac{1}{N} \sum_{i=1}^N (M_i - O_i)$$
 (1)

$$RMSE = \sqrt{\frac{1}{N-1} \sum_{i=1}^N (M_i - O_i)^2}$$
 (2)

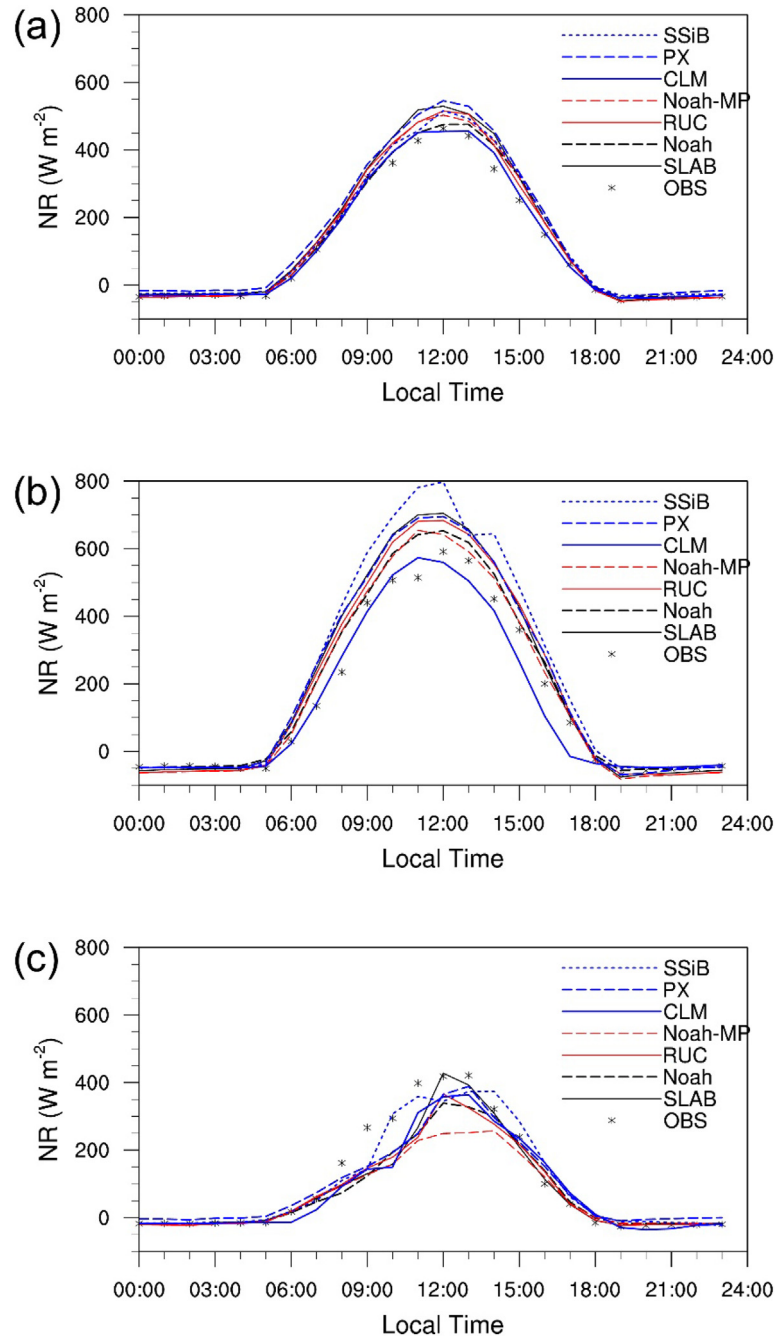


Fig. 2. The observed and simulated diurnal variations of net radiation (NR), averaged for the observational period (P1) (a), the SASM south phase (P2) (b), and the SASM north phase (P3) (c).

$$COR = \frac{\frac{1}{N} \sum_{i=1}^N (M_i - \bar{M})(O_i - \bar{O})}{\sqrt{\frac{1}{N} \sum_{i=1}^N (M_i - \bar{M})^2} \sqrt{\frac{1}{N} \sum_{i=1}^N (O_i - \bar{O})^2}} \quad (3)$$

where M_i and O_i is the simulated and observed variable, respectively.

2.2. Observational data

The data used in this study were obtained from an observation campaign named “Observation on the Surface-to-air Exchange Processes in Southeast Tibet” (OSEP). During the OSEP campaign, the land-atmosphere exchange fluxes, as well as the near-surface parameters, were measured at the Yarlung Tsangpo River Valley (29.449°N, 94.691°E, 2973 m), Southeast Tibet, from 20 May to July 9, 2013. Fig. 1a shows the topography of the OSEP observational domain. In this

region, the East Himalayas elongates from west to east, with a main ridge elevation of around 5000 m, and the Yarlung Tsangpo River rushes eastward in the north of the East Himalayas, with a water surface elevation of around 2900 m. The valley floor has a width of around 3 km, and the valley surface is mainly covered by typical grassland (with the grassland area of 30.6% within the observational domain), with scattered *Rosa multiflora thumb*, cropland with irrigated *hulleless barley*, and forests of *Quercus spinose*, *Pinus densata*, *Pices*, and *Abies* on the slopes. In this study, observational data at the grassland site (denoted by a black star in Fig. 1a) were used to evaluate the different LSSs. The land-atmosphere exchange data were collected by an eddy covariance system installed 2.2 m above the ground level (AGL) with a 3-D ultrasonic anemometer (Gill Windmaster Pro, Gill Instruments, Inc., UK) and a CO₂/H₂O infrared gas analyzer (LI7500A, Li-Cor Inc., USA).

Table 2

Statistical values of NR for the mean values (MEAN), MB, RMSE, and COR between the seven LSSs in WRF and the observations during the P1, P2 and P3 periods.

Variable		OBS	SLAB	Noah	RUC	Noah-MP	CLM	PX	SSiB
NR (P1)	MEAN	115	142	130	133	132	121	153	138
	MB	–	27	15	18	17	6	38	23
	RMSE	–	122	110	119	118	126	125	140
	COR	–	0.87	0.87	0.85	0.86	<i>0.83</i>	0.86	<i>0.82</i>
NR (P2)	MEAN	148	194	181	188	169	135	199	223
	MB	–	47	33	41	22	-13	51	75
	RMSE	–	124	104	119	107	152	125	154
	COR	–	0.92	0.93	0.92	0.92	<i>0.81</i>	0.92	<i>0.91</i>
NR (P3)	MEAN	105	84	79	79	67	82	95	100
	MB	–	-21	-26	-26	-38	-23	-10	-5
	RMSE	–	83	80	90	<i>104</i>	99	82	142
	COR	–	0.88	0.91	0.87	0.84	<i>0.83</i>	0.88	<i>0.70</i>

The bold and italicized numbers indicate good and poor performances, respectively.

The data's sample frequency was 10 Hz. The near surface radiation fluxes were collected by a 4-component net radiometer (NR01, Hukseflux Thermal Sensors, Netherlands), installed at 1.5 m AGL. The soil heat fluxes (HFP01, Hukseflux Thermal Sensors, Netherlands) were measured at a depth of 2 cm.

The turbulent sensible and latent heat fluxes were calculated by the EddyPro software v6.1.0 (Li-Cor Inc., Lincoln, NE, USA) at an interval of 30 min. Planar fitting for tilt correction was conducted during the processing. The surface temperature (T_s) was estimated as Eq. (4)

$$T_s = \left[\frac{ULR - (1 - \varepsilon)DLR}{\varepsilon\sigma} \right]^{0.25} \quad (4)$$

where ULR and DLR are the upward and downward longwave radiation fluxes, respectively. ε is the emissivity, and σ is the Stefan-Boltzmann constant. The surface soil heat flux (G_0) was calculated as Eqs. (5) and (6) (McCumber and Pielke, 1981; Chen and Dudhia, 2001),

$$G_0 = G_1 + C_s z \frac{\partial T}{\partial t} \quad (5)$$

$$C_s = (1 - \eta_s)C_d + \eta C_w, \quad (6)$$

where z is the depth (2.0 cm in this study) of the soil heat flux obtained, G_1 the soil heat flux at depth z , T the average soil temperature between the surface and z , C_s the soil volume heat capacity, η_s the soil porosity, η the volumetric moisture content, and C_d and C_w are the volumetric heat capacities for dry soils and water, respectively.

Studies have shown that surface energy is not balanced over the TP, i.e., the sum of the measured sensible, latent, and ground surface heat fluxes is less than the net radiation (Ma et al., 2005; Ma and Zhou, 2017). However, in numerical models these fluxes are balanced. Therefore, a Bowen ratio closure method (Twine et al., 2000) was used to correct the sensible and latent heat flux, which assumes the observed Bowen ratio is correct and adjusts the available energy (the net radiation flux minus the ground surface heat flux).

3. Results

During the OSEP campaign, the South Asia summer monsoon (SASM) began on June 1, 2013, and experienced a south phase during June 11–16 and then a north phase during June 26–30 (Zhou et al., 2015). During these phases, the SASM's large-scale circulations could bring different air flows to the Southeast Tibet and affected the local atmospheric parameters and land-atmosphere exchange processes (Zhou et al., 2015). To evaluate WRF LSSs under different synoptic situations, we investigated the energy components' variations during the whole observational period (denoted by P1 hereafter), the SASM south phase (P2) and north phase (P3).

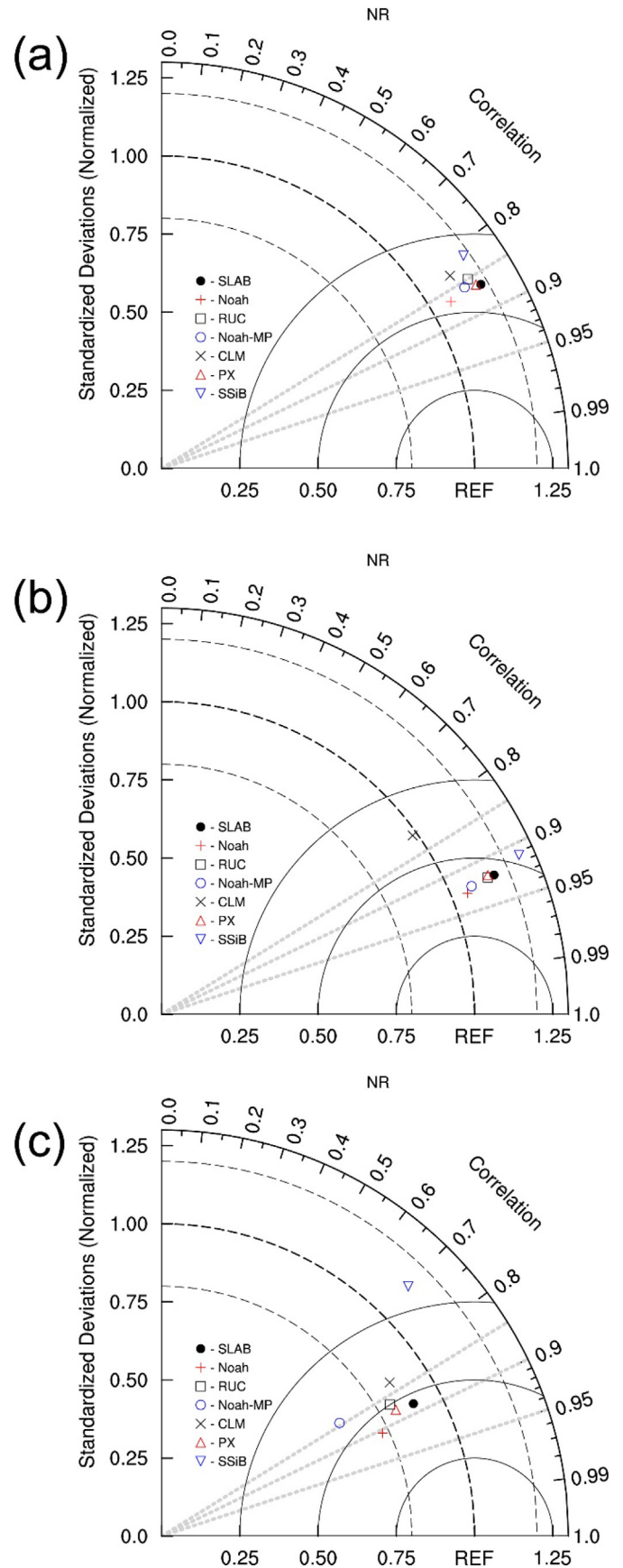


Fig. 3. Taylor diagrams of net radiation (NR) for P1 (a), P2 (b), and P3 (c).

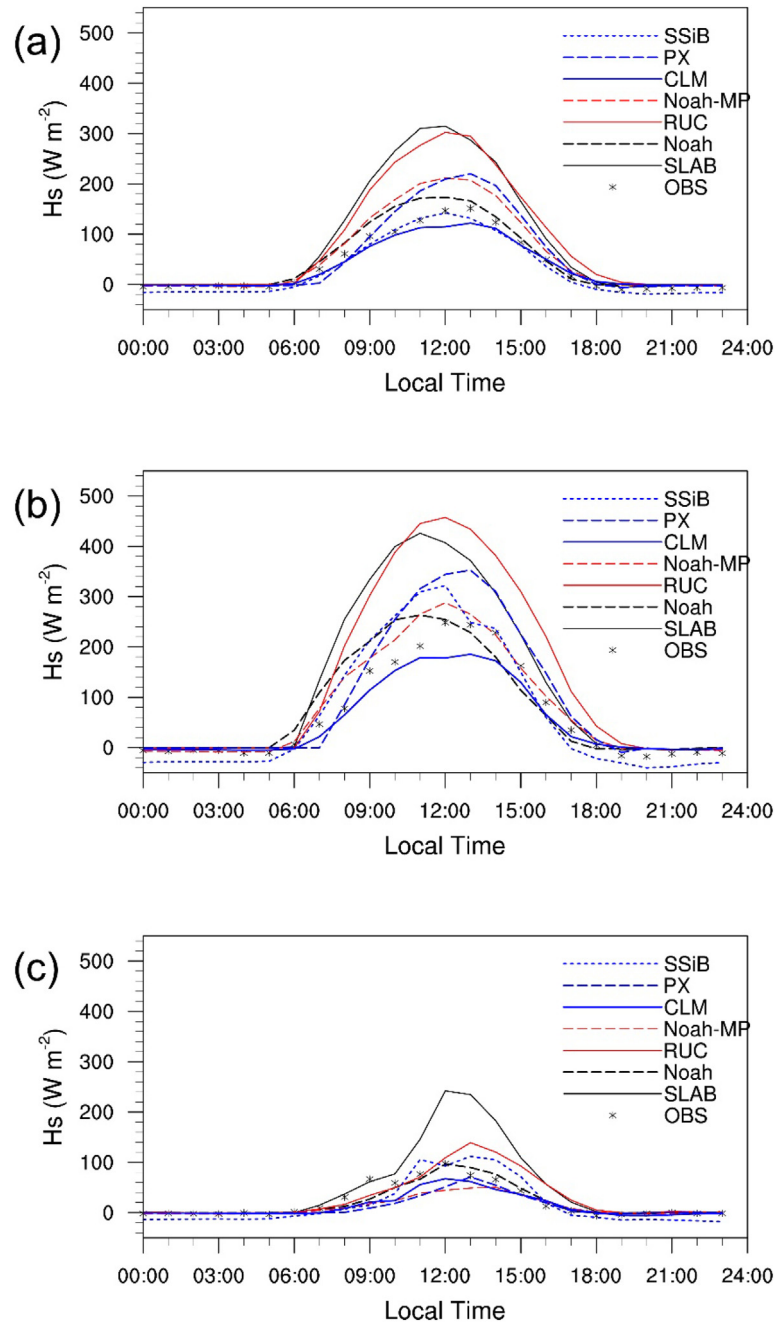


Fig. 4. The observed and simulated diurnal variations of sensible heat flux (H_s), averaged for P1 (a), P2 (b) and P3 (c).

From the energy balance equation, the received energy (net radiation, NR) can be balanced by the land-atmosphere heat transfers, including the sensible heat flux (H_s), latent heat flux (LE) and ground surface flux (G_0), as shown in Eq. (7),

$$NR = H_s + LE + G_0 \quad (7)$$

In the following, the land-atmosphere heat transfers, as well as the net radiation flux, is calculated in the above three periods.

3.1. Net radiation flux

The net radiation flux (NR) is the summary of the incoming and outgoing short- and long-wave radiation fluxes (Eq. (8)), with the positive/negative values representing the net heating/cooling to the near-surface atmosphere.

$$NR = DR - UR + DLR - ULR \quad (8)$$

Fig. 2 shows the diurnal variations of net radiation from the observation and all LSSs, which are averaged for the P1 (Fig. 2a), P2 (Fig. 2b) and P3 (Fig. 2c) periods, respectively. It is clearly seen from the figure that the diurnal variations of NR can be well simulated by all LSSs, i.e., net heating occurred at daytime (positive NR values) with the maximum at noon, and net cooling (negative NR value) at night with the minimum at early morning. The large NR variations among different synoptic situations are also well simulated by all LSSs, i.e., the high NR during the SASM south phase (P2) and the low value during the SASM north phase (P3), but with different amplitudes.

To assess the different performances of all LSSs in simulating the NR , statistical analyses were conducted, including the mean bias (MB), residual mean square error ($RMSE$) and correlation coefficient (COR) between the LSSs and observations calculated and listed in Table 2. As a

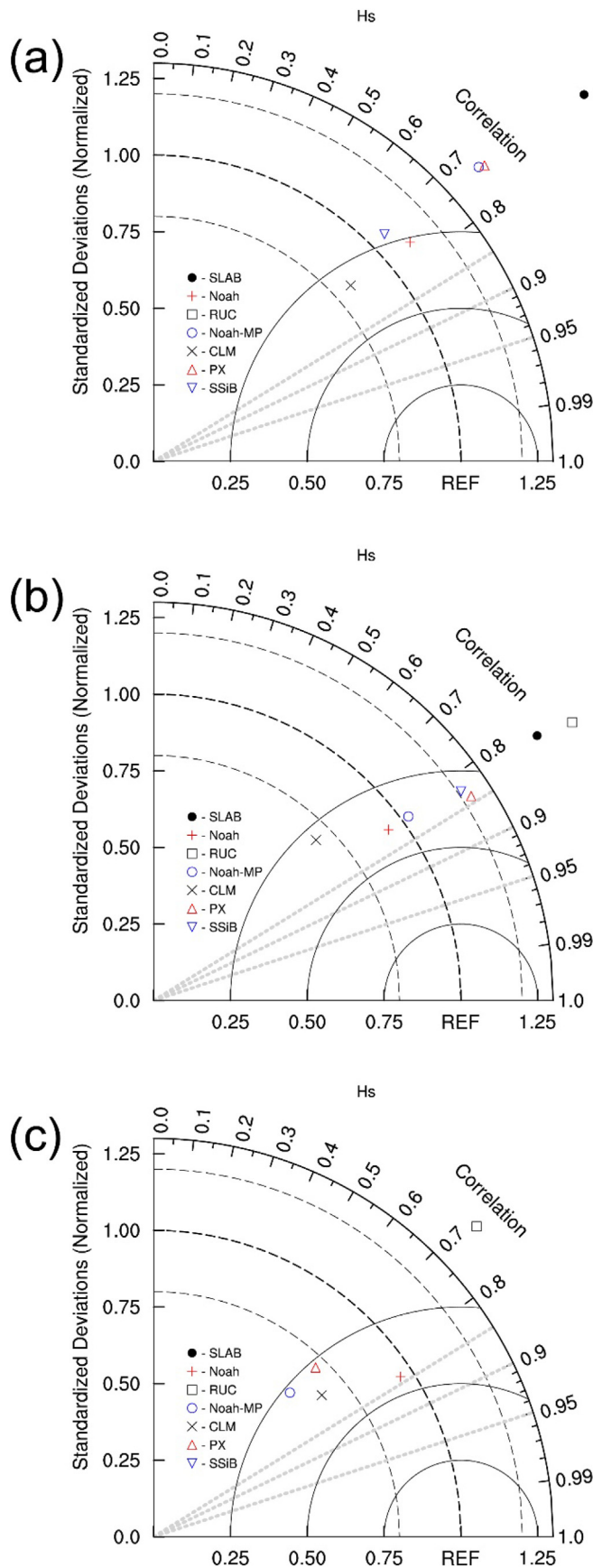


Fig. 5. Taylor diagrams of sensible heat flux (H_s) for P1 (a), P2 (b), and P3 (c).

Table 3

Statistical values of H_s for the mean values (MEAN), MB, RMSE, and COR between the seven LSSs in WRF and the observations in P1, P2 and P3.

Variable		OBS	SLAB	Noah	RUC	Noah-MP	CLM	PX	SSiB
H_s (P1)	MEAN	39	88	51	87	60	35	53	29
	MB	–	49	12	48	21	–4	16	–10
	RMSE	–	105	55	105	74	52	72	59
	COR	–	0.76	0.76	0.77	0.74	0.74	0.74	0.71
H_s (P2)	MEAN	65	126	79	140	80	52	95	68
	MB	–	62	14	75	15	–13	30	3
	RMSE	–	114	66	128	68	76	77	71
	COR	–	0.82	0.81	0.83	0.81	0.71	0.84	0.83
H_s (P3)	MEAN	22	50	21	31	12	13	12	17
	MB	–	28	–1	9	–10	–8	–9	–5
	RMSE	–	67	21	39	29	25	28	64
	COR	–	0.84	0.84	0.72	0.69	0.76	0.69	0.52

The bold and italicized numbers indicate good and poor performances, respectively.

visual picture, Taylor diagrams (Taylor, 2001) are also applied to this study, which illustrates the NR in the three periods derived from COR and SD ratio between the LSSs and observation (Fig. 3). In Fig. 3, the dashed arc marked “REF” indicates the observation, and the distances from “REF” indicate the relative performances of LSSs. During the observational period (P1) (see Figs. 2a and 3a), all LSSs overestimate NR. Given all statistical parameters in Table 2, the Noah scheme performs best in retrieving the NR, with the smallest MB (15 W m^{-2}) and RMSE (110 W m^{-2}) and largest COR (0.87). The good performance of Noah scheme can be closely related to the surface temperature variation, which is discussed in the following. During the SASM south phase (P2) (see Figs. 2b and 3b), all LSSs but CLM overestimate NR. The Noah and Noah-MP schemes are the best among all LSSs, with smaller MB (33 W m^{-2} for Noah and 22 W m^{-2} for Noah-MP) and RMSE (104 W m^{-2} for Noah and 107 W m^{-2} for Noah-MP) and largest COR (0.93 for Noah and 0.92 for Noah-MP). During the SASM north phase (P3) (see Figs. 2c and 3c), all LSSs except SSiB underestimated the NR, which may indicate most of the LSSs overestimated the cloud amount during the SASM north phase period (Zhou et al., 2015). The Noah and PX schemes performed the best among all LSSs, with smaller MB (-26 W m^{-2} for Noah and -9 W m^{-2} for PX) and RMSE (80 W m^{-2} for Noah and 82 W m^{-2} for PX) and largest COR (0.91 for Noah and 0.88 for PX).

Therefore, the WRF Noah is the best scheme among all the seven LSSs in retrieving the observed NR variations in the Southeast Tibet, even under the different synoptic situations.

3.2. Sensible heat flux

Fig. 4 shows the diurnal variations of sensible heat fluxes (H_s) from the observation and all LSSs simulated results, averaged for P1 (Fig. 4a), P2 (Fig. 4b) and P3 (Fig. 4c), respectively. From the figure, the diurnal variations of H_s can be well simulated by all LSSs, with small negative values at night and positive values in the daytime. The simulated H_s is larger in the SASM south phase (P2) than that in the SASM north phase (P3), which is consistent with the observations.

Similar as NR, the Taylor diagram is also presented to evaluate the LSSs performances in retrieving the H_s (see Fig. 5). In addition, all the statistical analyses were also conducted to obtain the MB, RMSE and COR and listed in Table 3. During the observational period (P1) (see Figs. 4a and 5a), all LSSs except CLM overestimate H_s . Given all statistical parameters in Table 3, the Noah, SSiB and CLM schemes perform better in retrieving the H_s , with the absolute MB values less than 12 W m^{-2} and RMSE less than 60 W m^{-2} . The large discrepancies for H_s between different LSSs, especially the larger overestimations from the SLAB and RUC schemes, have been documented by previous studies, which could be related to the soil moisture conditions (e.g., Zeng et al.,

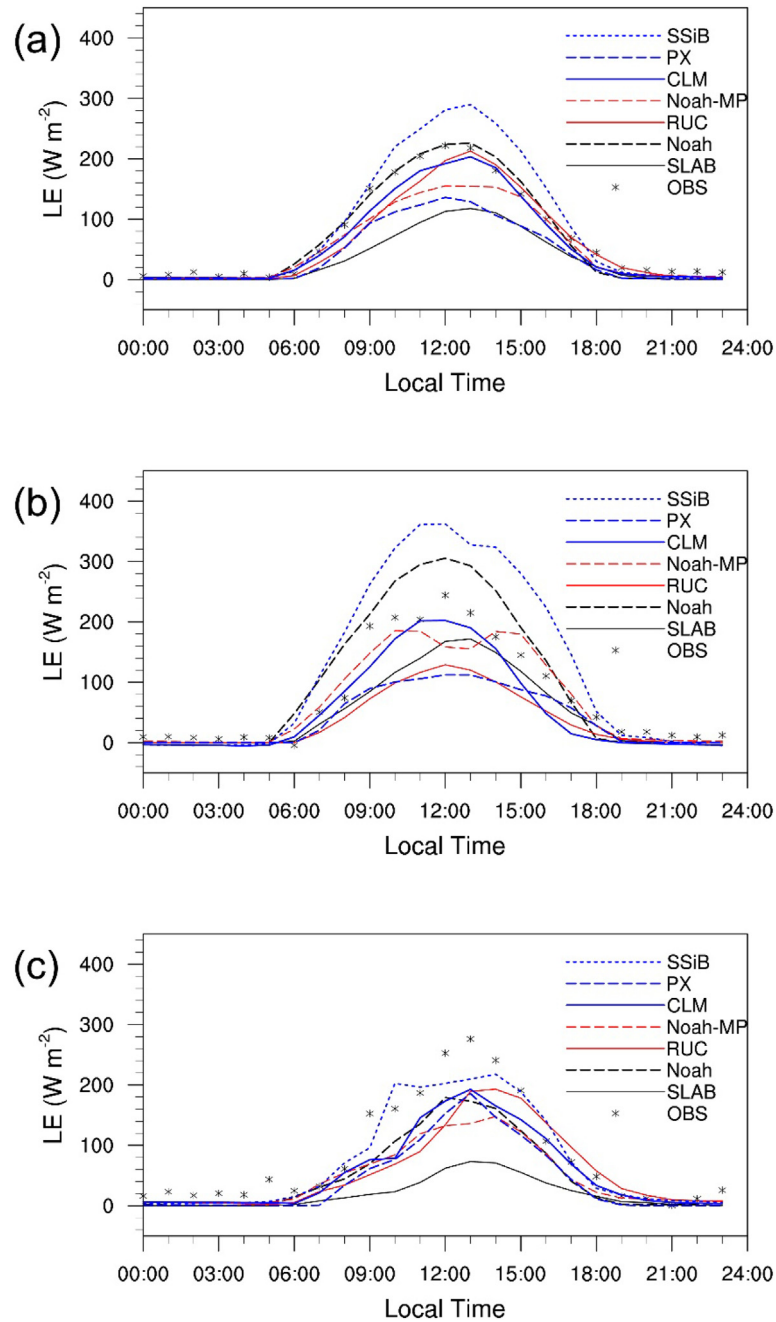


Fig. 6. The observed and simulated diurnal variations of latent heat flux (LE), averaged for P1 (a), P2 (b), and P3 (c).

2015). During the SASM south phase (P2) (see Figs. 4b and 5b), all LSSs but CLM and Noah overestimate H_s . The Noah and Noah-MP schemes are the best among all LSSs, with smaller MB (14 W m^{-2} for Noah and 15 W m^{-2} for Noah-MP) and $RMSE$ (66 W m^{-2} for Noah and 68 W m^{-2} for Noah-MP). During the SASM north phase (P3) (see Figs. 4c and 5c), all LSSs except RUC underestimated the H_s , which could be closely related to the underestimation of NR and surface-to-air temperature contrast (see discussions in the following) during the SASM north phase period. The Noah scheme performed the best among all LSSs, with smallest MB (0 W m^{-2}) and $RMSE$ (21 W m^{-2}) and largest COR (0.84).

Therefore, the WRF Noah is the best scheme among all the seven LSSs in retrieving the H_s variations in the Southeast Tibet during three periods, and the SSiB, Noah-MP and CLM performs better during the whole observation period, SASM south and north periods, respectively.

3.3. Latent heat flux

Fig. 6 shows the diurnal variations of latent heat fluxes (LE) from the observation and all LSSs simulation results, averaged for P1 (Fig. 6a), P2 (Fig. 6b) and P3 (Fig. 6c), respectively. From the figure, the diurnal variations of LE can be well simulated by all LSSs, with small negative values at night and positive values in the daytime. The simulated LE is larger in the SASM south phase (P2) than that in the SASM north phase (P3), which is consistent with previous studies (Zhou et al., 2015).

Fig. 7 presents the Taylor diagram of LE , and all the statistical parameters were calculated and listed in Table 4. During the observational period (P1) (see Figs. 6a and 7a), the LE was well simulated by the Noah, CLM and RUC schemes, while largely overestimated by SSiB and underestimated by the other three schemes. In fact, the bad performances of four LSSs have been reported in the previous studies,

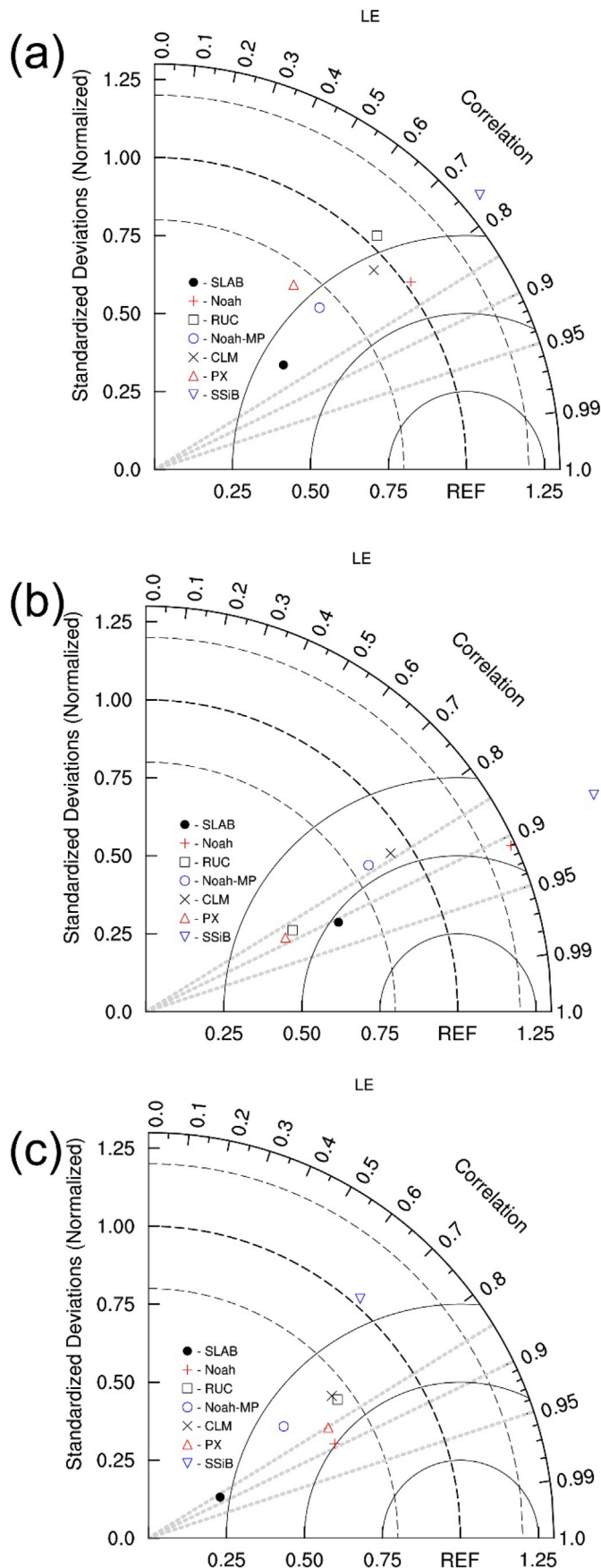


Fig. 7. Taylor diagrams of latent heat flux (LE) for P1 (a), P2 (b), and P3 (c).

Table 4

Statistical values of LE for the mean values (MEAN), MB, RMSE, and COR between the seven LSSs in WRF and the observations during P1, P2, and P3.

Variable		OBS	SLAB	Noah	RUC	Noah-mp	CLM	PX	SSiB
LE (P1)	MEAN	74	35	72	63	57	63	42	90
	MB	-	-39	-2	-11	-17	-11	-31	16
	RMSE	-	74	58	75	67	66	82	83
	COR	-	0.78	0.81	0.69	0.71	0.74	0.60	0.76
LE (P2)	MEAN	77	50	98	37	69	55	40	124
	MB	-	-27	21	-40	-8	-22	-37	47
	RMSE	-	51	55	67	50	58	66	87
	COR	-	0.90	0.91	0.87	0.84	0.84	0.88	0.90
LE (P3)	MEAN	85	20	51	58	48	57	43	74
	MB	-	-65	-34	-27	-37	-28	-42	-11
	RMSE	-	102	61	65	76	68	68	87
	COR	-	0.87	0.89	0.81	0.77	0.79	0.85	0.66

The bold and italicized numbers indicate good and poor performances, respectively.

mainly caused by the incorrect moisture conditions (Dudhia, 1996; Xiu and Pleim, 2001; Miao et al., 2007). Among all LSSs, the Noah scheme performs best in retrieving the LE , with the MB value of -2 W m^{-2} , RMSE 58 W m^{-2} and the COR of 0.81. During the SASM south phase (P2), it seems that the CLM, Noah and Noah-MP perform better than the other LSSs in the LE simulations from both Fig. 6b and Table 4, with the absolute MB values less than 22 W m^{-2} and RMSE less than 58 W m^{-2} . During the SASM north phase (P3) (see Figs. 6c and 7c), all LSSs except SSiB underestimated the LE , which could also be related to the underestimation of NR and surface-to-air temperature contrast during the SASM north phase period. The Noah scheme performed the best among all LSSs, with a smaller MB value (-34 W m^{-2}) and the smallest RMSE (61 W m^{-2}) and largest COR (0.89).

Therefore, the WRF Noah is the best scheme among all the seven LSSs in retrieving the LE variations in the Southeast Tibet during all three periods, and the CLM, Noah-MP and RUC performs better during the whole observation period, SASM south and north periods, respectively.

4. Discussions

In previous sections, the net radiation, sensible and latent heat flux have been compared with different WRF LSSs in the Southeast Tibet. To illustrate the overall simulating results, the ground heat flux (GO) was calculated from Eq. (8). Fig. 8 shows the diurnal variation of GO during the observational period (P1). The ground heat flux was slightly underestimated by Noah scheme but overestimated by all the other schemes. Statistical analyses (see Table 5) also suggested that the Noah scheme performs the best, which is consistent with the above results.

From the above, all LSSs simulations successfully captured the diurnal variations of observed land-atmosphere heat transfers, but with large discrepancies in magnitude. To investigate the possible reasons, the simulated surface temperature (T_s) was firstly examined, which are directly related with the different land schemes. Fig. 9 presents the diurnal variations of observed and simulated surface temperatures, averaged for the observational period. From the figure, the diurnal variations of surface temperatures can be well simulated by all LSSs, with an increase in the morning and a decrease in the afternoon. However, the magnitude of T_s is largely underestimated by all LSSs, in which the WRF Noah is the best scheme to reproduce the observed surface temperature. The well simulated T_s from WRF Noah scheme could be greatly attributed to the retrieved net radiation flux (NR) in Fig. 2a and Table 2, by affecting the long-wave radiation flux. In addition, the accurate T_s could also contribute to the land-atmosphere heat transfers, which are driven by the temperature contrast between the surface and air (see Fig. 10 and Table 6). From the above figures and tables, it is clearly seen that the Noah scheme performs the best in

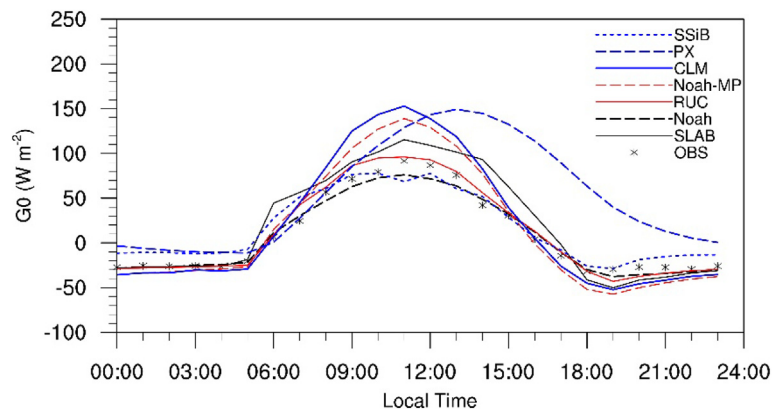


Fig. 8. The observed and simulated diurnal variations of the ground heat flux (G_0), averaged for the observational period (P1).

Table 5
Statistical values of G_0 for the mean values (*MEAN*), *MB*, *RMSE*, and *COR* between the seven LSSs in WRF and the observations during P1.

Variable		OBS	SLAB	Noah	RUC	Noah-MP	CLM	PX	SSiB
G_0 (P1)	MEAN	9.75	20.22	6.93	12.02	14.70	19.41	53.25	16.70
	MB	-	10.48	-2.82	2.29	4.95	9.66	<i>43.50</i>	6.95
	RMSE	-	41.25	28.30	31.58	44.92	53.98	<i>65.26</i>	36.87
	COR	-	0.80	0.83	0.82	0.82	0.80	<i>0.69</i>	<i>0.71</i>

The bold and italicized numbers indicate good and poor performances, respectively.

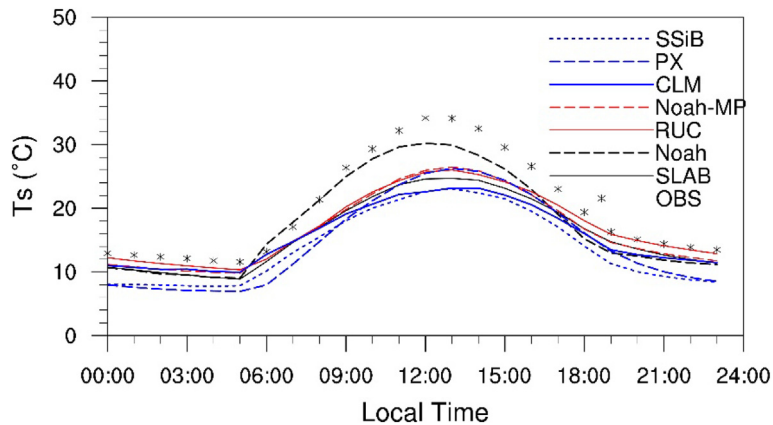


Fig. 9. The observed and simulated diurnal variation of surface temperature (T_s), averaged for the observational period (P1).

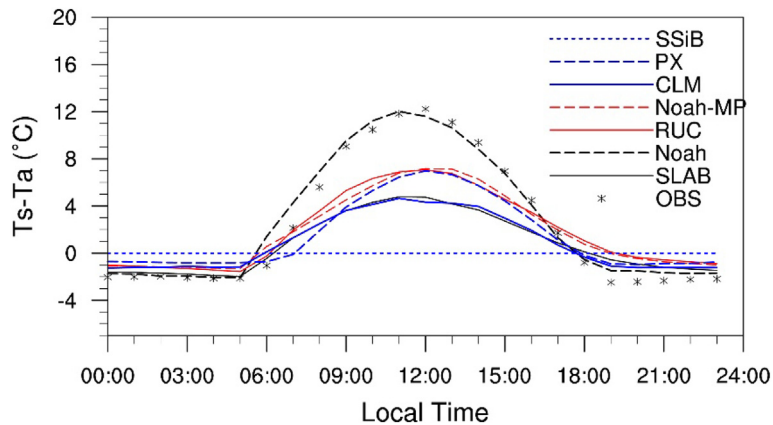
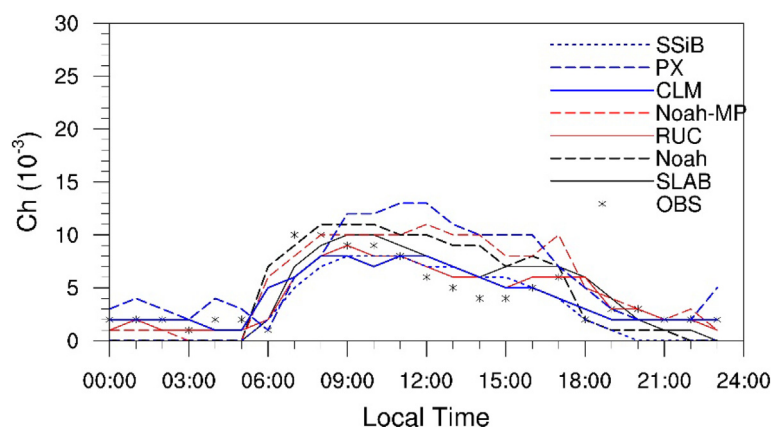


Fig. 10. The observed and simulated diurnal variations of temperature differences between the surface and air at 2 m AGL (T_s-T_a) averaged for P1.

Table 6Statistical values of T_s - T_a for the mean values (*MEAN*), *MB*, *RMSE*, and *COR* between the seven LSSs in WRF and the observations during P1.

Variable		OBS	SLAB	Noah	RUC	Noah-mp	CLM	PX	SSiB
T_s - T_a (P1)	<i>MEAN</i>	2.46	0.76	2.86	1.86	1.82	0.87	1.47	–
	<i>MB</i>	–	–1.71	0.39	–0.60	–0.64	–1.59	–0.99	–
	<i>RMSE</i>	–	4.73	3.51	3.92	3.95	4.63	4.06	–
	<i>COR</i>	–	0.82	0.84	0.83	0.82	0.81	0.83	–

The bold and italicized numbers indicate good and poor performances, respectively.

**Fig. 11.** The observed and simulated diurnal variation of bulk heat transfer coefficients (C_h), averaged for the observational period (P1).

capturing the temperature contrast, with the smallest *MB* (0.39 °C), *RMSE* (3.51 °C) and the largest *COR* (0.84).

Another possible factor affecting the heat transfer is the bulk heat transfer coefficients (C_h), with its diurnal variation presented in Fig. 11. Most of LSSs overestimated the observed C_h , despite of well simulated diurnal variations. Statistical analyses (not shown) suggested that the difference of C_h obtained from all the seven LSSs is negligible, although the WRF SSiB is a little superior than the others (Yang et al., 2009). Therefore, the surface temperature can be the dominant factor affecting the simulated land-atmosphere heat transfer, through adjusting driving forces such as the radiation irradiance and the thermal contrasts between the surface and air.

5. Conclusions

In this study, we evaluated the performances of seven WRF land surface schemes (LSSs) in simulating the land-atmosphere exchange processes in the Southeast Tibet. The simulated surface net radiation, sensible and latent heat fluxes were compared with those measured over grassland surfaces during the OSEP campaign from May 20 to July 9, 2013. Statistical analyses also adopted to assess every LSS under different synoptic situations, including the SASM south and north phases. All the WRF LSSs can successfully reproduce the diurnal variations of the land-atmosphere heat transfer during the whole observational period, the SASM south and north phases. However, large magnitude differences exist within the LSSs simulations comparing with the observed values, which make the optimal scheme selection difficult. For example, the net radiation flux (*NR*) and sensible heat flux (*H_s*) were overestimated by most of LSSs during the observational and SASM south periods, however, they were underestimated by all most of LSSs during the SASM north phase. The latent heat flux was well simulated by the Noah, CLM and RUC schemes, while largely overestimated by SSiB scheme and underestimated by the other three schemes during the observational period. It was underestimated by all LSSs except SSiB scheme during the SASM north phase. To quantitatively evaluate each scheme, statistical analyses were conducted by calculations of mean bias, residual mean square error, and the correlation coefficient. The results showed that the WRF-Noah scheme performs the best among all

WRF LSSs in retrieving the land-atmosphere heat transfer. The most successfully simulated surface temperature from WRF-Noah scheme can be a dominant factor to affect the land-atmosphere heat transfer, through adjusting the bulk transfer coefficient for heat and water vapor and thermal contrast between the surface and air. Therefore, the WRF-Noah scheme is strongly recommended for future land-atmosphere exchange studies over the Southeast Tibet.

This study provides a quantitative evaluation of commonly used LSSs in simulating land-atmosphere exchange processes over grassland surfaces in the Southeast Tibet. Further evaluations with extended observational data still need to be conducted over other surface covers, including forests, and croplands, et al. The results also indicate the land surface schemes have large bias in the land-atmosphere interaction simulations in the TP, and need to be revised according to more high quality in situ dataset.

Declaration of Competing Interest

The authors declare that they have no known competing financial interests or personal relationships that could have appeared to influence the work reported in this paper.

Acknowledgements

This study is supported by “the Strategic Priority Research Program of the Chinese Academy of Sciences” (Grant No. XDA19070401), National Natural Science Foundation of China (Grant No. 41830968), and the CAS Key Subordinate Project (Grant No. KGFZD-135-16-023). We appreciate the access of the GLDAS data sets at NASA Goddard Earth Science Data Information and Services Center, and the CFSV2 data sets at NCEP /NCAR.

References

- Benjamin, S.G., Grell, G.A., Brown, J.M., et al., 2004. Mesoscale weather prediction with the RUC hybrid isentropic-terrain-following coordinate model. *Mon. Weather Rev.* 132, 473–494.
- Chen, F., Dudhia, J., 2001. Coupling an advanced land surface–hydrology model with the Penn State–NCAR MM5 modeling system. Part I: model implementation and

- sensitivity. *Mon. Weather Rev.* 129, 569–585.
- Chen, Y., Yang, K., Qin, J., et al., 2013. Evaluation of AMSR-E retrievals and GLDAS simulations against observations of a soil moisture network on the central Tibetan Plateau. *J. Geophys. Res. Atmos.* 118, 4466–4475. <https://doi.org/10.1002/jgrd.50301>.
- Duan, A., Wu, G., 2008. Weakening trend in the atmospheric heat source over the Tibetan Plateau during recent decades. Part I: observations. *J. Clim.* 21 (13), 3149–3164.
- Dudhia, J., 1996. A Multi-layer Soil Temperature Model for MM5. The Sixth PSU/NCAR MM5 Users' Workshop, Boulder, Colorado.
- Gao, Y., Xiao, L., Chen, D., et al., 2017. Quantification of the relative role of land-surface processes and large-scale forcing in dynamic downscaling over the Tibetan Plateau. *Clim. Dyn.* 48 (5–6), 1705–1721.
- Hong, S.-Y., Noh, Y., Dudhia, J., 2006. A new vertical diffusion package with an explicit treatment of entrainment processes. *Mon. Weather Rev.* 134, 2318–2341. <https://doi.org/10.1175/MWR3199.1>.
- Hong, S., Lakshmi, V., Small, E.E., et al., 2009. Effects of vegetation and soil moisture on the simulated land surface processes from the coupled WRF/Noah model. *J. Geophys. Res.* 114, D18118. <https://doi.org/10.1029/2008JD011249>.
- Iacono, M.J., Delamere, J.S., Mlawer, E.J., et al., 2008. Radiative forcing by long-lived greenhouse gases: calculations with the AER radiative transfer models. *J. Geophys. Res.* 113, D13103.
- Jiménez, P., Dudhia, J., González-Rouco, J., et al., 2012. A revised scheme for the WRF surface layer formulation. *Mon. Weather Rev.* 140, 898–918.
- Jin, J., Miller, N.L., Schlegel, N., 2010. Sensitivity study of four land surface schemes in the WRF model. *Adv. Meteorol.* 167436. <https://doi.org/10.1155/2010/167436>.
- Kain, J.S., 2004. The Kain–Fritsch convective parameterization: an update. *J. Appl. Meteorol.* 43, 170–181.
- Lawrence, D.M., Oleson, K.W., Flanner, M.G., et al., 2011. Parameterization improvements and functional and structural advances in version 4 of the community land model. *J. Adv. Model. Earth Syst.* 3, M03001. <https://doi.org/10.1029/2011MS000045>.
- Lin, T., Cheng, F., 2016. Impact of soil moisture initialization and soil texture on simulated land–atmosphere interaction in Taiwan. *J. Hydrometeorol.* 17 (5), 1337–1355.
- Liu, C., Yu, Y., Xie, J., et al., 2015. Applicability of soil temperature and moisture in several dataset over qinghai-xizang plateau. *Plateau Meteorol.* 34 (3), 653–665 in Chinese.
- Ma, S., Zhou, L., 2017. Characteristics of land-atmosphere exchange parameters over grassland in Southeast Tibet. *J. Hydrometeorol.* 18, 2249–2264. <https://doi.org/10.1175/JHM-D-16-0084.1>.
- Ma, Y., Fan, S., Ishikawa, H., et al., 2005. Diurnal and inter-monthly variation of land surface heat fluxes over the central Tibetan Plateau area. *Theor. Appl. Climatol.* 80 (2–4), 259–273.
- Mass, C., Owens, D., 2011. Fixing WRF's high speed wind bias: a new subgrid scale drag parameterization and the role of detailed verification. In: In 24th Conference on Weather and Forecasting and 20th Conference on Numerical Weather Prediction. Preprint, 91st American Meteorological Society Annual Meeting.
- Maussion, F., Scherer, D., Finkelnburg, R., et al., 2011. WRF simulation of a precipitation event over the Tibetan Plateau, China—an assessment using remote sensing and ground observations. *Hydrol. Earth Syst. Sci.* 15 (6), 1795–1817.
- McCumber, M.C., Pielke, R.A., 1981. Simulation of the effects of surface fluxes of heat and moisture in a mesoscale numerical model. Part I: soil layer. *J. Geophys. Res.* 86, 9929–9938.
- Miao, J.F., Chen, D., Borne, K., 2007. Evaluation and comparison of noah and pleim-xiu land surface models in MM5 using GÖTE2001 data: spatial and temporal variations in near-surface air temperature. *J. Appl. Meteorol. Climatol.* 46 (10), 1587–1605.
- Miao, S., Chen, F., LeMone, M., et al., 2009. An observational and modeling study of characteristics of urban heat island and boundary layer structures in Beijing. *J. Appl. Meteorol. Climatol.* 48 (3), 484–501.
- Niu, G.Y., Yang, Z.L., Mitchell, K.E., et al., 2011. The community Noah land surface model with multiparameterization options (Noah-MP): 1. Model description and evaluation with local-scale measurements. *J. Geophys. Res. Atmos.* 116 (D12). <https://doi.org/10.1029/2010JD015139>.
- Pleim, J.E., Xiu, A., 1995. Development and testing of a surface flux and planetary boundary layer model for application in mesoscale models. *J. Appl. Meteorol.* 34, 16–32.
- Porter, D.F., Cassano, J.J., Serreze, M.C., 2012. Local and large-scale atmospheric responses to reduced Arctic Sea ice and ocean warming in the WRF model. *J. Geophys. Res.* 117, D11115. <https://doi.org/10.1029/2011JD016969>.
- Rodell, M., Houser, P.R., Jambor, U., et al., 2004. The global land data assimilation system. *Bull. Amer. Meteor. Soc.* 85 (3), 381–394. <https://doi.org/10.1175/BAMS-85-3-381>.
- Saha, S., et al., 2011. NCEP climate forecast system version 2 (CFSv2) 6-hourly products. In: Research Data Archive at the National Center for Atmospheric Research. Computational and Information Systems Laboratory. <https://doi.org/10.5065/D61C1TXF>.
- Skamarock, W., Klemp, J., Dudhia, J., et al., 2008. A Description of the Advanced Research WRF Version 3. NCAR Tech. Note.
- Tao, S.Y., Chen, L.S., Xu, X.D., et al., 1999. Progresses of Theoretical Study in the Second Tibetan Plateau Atmosphere Scientific Experiment (Part I). China Meteorology Press, Beijing (in Chinese).
- Taylor, K.E., 2001. Summarizing multiple aspects of model performance in a single diagram. *J. Geophys. Res. Atmos.* 106 (D7), 7183–7192.
- Thompson, G., Field, P.R., Rasmussen, R.M., et al., 2008. Explicit forecasts of winter precipitation using an improved bulk microphysics scheme. Part II: implementation of a new snow parameterization. *Mon. Weather Rev.* 136, 5095–5115. <https://doi.org/10.1175/2008MWR2387.1>.
- Twine, T.E., Kustas, W.P., Norman, J.M., et al., 2000. Correcting eddy-covariance flux underestimates over a grassland. *Agric. For. Meteorol.* 103 (3), 279–300.
- Wu, G., Zhang, Y., 1998. Tibetan Plateau forcing and the timing of the monsoon onset over South Asia and the South China Sea. *Mon. Weather Rev.* 126 (4), 913–927.
- Wu, G., Liu, Y., Wang, T., et al., 2007. The influence of mechanical and thermal forcing by the Tibetan Plateau on Asian climate. *J. Hydrometeorol.* 8 (4), 770–789.
- Wu, G.X., Liu, Y.M., Bian, H., et al., 2012. Thermal controls on the Asian summer monsoon. *Sci. Rep.* 2 (404). <https://doi.org/10.1038/srep00404>.
- Wu, G., He, B., Duan, A., et al., 2017. Formation and variation of the atmospheric heat source over the Tibetan Plateau and its climate effects. *Adv. Atmos. Sci.* 34 (10), 1169–1184.
- Xiu, A., Pleim, J.E., 2001. Development of a land surface model. Part I: application in a mesoscale meteorological model. *J. Appl. Meteorol.* 40, 192–209.
- Xu, L., Liu, H., Du, Q., et al., 2019. The assessment of the planetary boundary layer schemes in WRF over the central Tibetan Plateau. *Atmos. Res.* 230, 104644. <https://doi.org/10.1016/j.atmosres.2019.104644>.
- Xue, Y., Sellers, P.J., Kinter, J.L., et al., 1991. A simplified biosphere model for global climate studies. *J. Clim.* 4, 345–364.
- Yang, K., Chen, Y.-Y., Qin, J., 2009. Some practical notes on the land surface modeling in the Tibetan Plateau. *Hydrol. Earth Syst. Sci.* 13, 687–701.
- Yang, Z., Dominguez, F., Zeng, X., et al., 2017. Impact of irrigation over the California central valley on regional climate. *J. Hydrometeorol.* 18 (5), 1341–1357.
- Ye, D., Gao, Y., 1979. Meteorology of the Qinghai-Xizang Plateau. Science Press, Beijing.
- Zeng, X.-M., Wang, N., Wang, Y., et al., 2015. WRF-simulated sensitivity to land surface schemes in short and medium ranges for a high-temperature event in East China: a comparative study. *J. Adv. Model. Earth Syst.* 7, 1305–1325. <https://doi.org/10.1002/2015MS000440>.
- Zhou, L.B., Zou, H., Ma, S.P., et al., 2011. Vertical air mass exchange driven by the local circulation on the northern slope of Mount Everest. *Adv. Atmos. Sci.* 28 (1), 217–222. <https://doi.org/10.1007/s00376-010-9231-z>.
- Zhou, L.B., Zou, H., Ma, S.P., et al., 2012. Observed impact of the South Asian summer monsoon on the local meteorology in the Himalayas. *Acta Meteorol. Sin.* 26 (2), 205–215. <https://doi.org/10.1007/s13351-012-0206-0>.
- Zhou, L., Zou, H., Ma, S., 2013. The Tibetan ozone low and its long-term variation during 1979–2010. *Acta Meteorol. Sin.* 27 (1), 75–86. <https://doi.org/10.1007/s13351-013-0108-9>.
- Zhou, L.B., Zou, H., Ma, S.P., et al., 2015. The observed impacts of South Asian summer monsoon on the local atmosphere and the near-surface turbulent heat exchange over the Southeast Tibet. *J. Geophys. Res. Atmos.* 120. <https://doi.org/10.1002/2014JD022928>.
- Zou, H., 1996. Seasonal variation and trends of TOMS ozone over Tibet. *Geophys. Res. Lett.* 23 (9), 1029–1032. <https://doi.org/10.1029/96GL00767>.
- Zou, H., Gao, Y., 1997. Vertical ozone profile over Tibet using Sage I and II data. *Adv. Atmos. Sci.* 14 (4), 505–512.
- Zou, H., Ma, S.P., Zhou, L.B., et al., 2009. Measured turbulent heat transfer on the northern slope of Mt. Everest and its relation to the south Asian summer monsoon. *Geophys. Res. Lett.* 36, L09810. <https://doi.org/10.1029/2008GL036984>.
- Zou, H., Li, P., Ma, S.P., et al., 2012. The local atmosphere and the turbulent heat transfer in the eastern Himalayas. *Adv. Atmos. Sci.* 29 (3), 435–440. <https://doi.org/10.1007/s00376-011-0233-2>.